AIAA Paper 2012-0039, 50th AIAA Aerospace Sciences Meeting,
9-12 Jan. 2012, Nashville, TN, USA

Prediction of a Supersonic Wing Flutter Boundary Using a High Fidelity Detached Eddy Simulation

Hong-Sik IM [*], Xiang-Yiang Chen[†], Ge-Cheng Zha[‡]
Dept. of Mechanical and Aerospace Engineering
University of Miami
Coral Gables, Florida 33124
E-mail: gzha@miami.edu

Abstract

Delayed Detached Eddy Simulation of supersonic flutter of a 3D wing is conducted at free stream Mach number of 1.141 using a fully coupled fluid/structure interaction (FSI). Unsteady 3D compressible Navier-Stokes equations are solved with a system of 5 decoupled structure modal equations in a fully coupled manner. The low diffusion E-CUSP scheme with a 5th order WENO reconstruction for the inviscid flux and a set of 4th order central differencing for the viscous terms are used to accurately capture the shock wave/turbulent boundary layer interaction of the vibrating wing. The predicted flutter boundary at supersonic Mach number achieves excellent agreement with experiment. It appears to be the first time that a numerical prediction of supersonic flutter boundary matches with experiment accurately.

Nomenclature

d	distance from the closest wall
f_d	delayed LES function in DDES
J	Jacobian of the coordinate transformation
I	identity matrix
ξ_t, η_t, ζ_t	ξ, η, ζ component of grid moving velocity
U, V, W	ξ, η, ζ component of contravariant velocity
$U_{i,j}$	velocity gradient
x, y, z	Cartesian coordinates
δ_{ij}	Kronecker delta
Pr	Prandtl number
Pr_t	turbulent Prandtl number
ν	kinematic viscosity
δ_x	x-component of displacements of the structure surface
δ_y	y-component of displacements of the structure surface
δ_z	z-component of displacements of the structure surface
ξ, η, ζ	generalized coordinates

Subscripts

i, j, k	indices
∞	reference variable at free stream

Flutter parameters

b_s	wing root semi-chord
$\bar{m}$	wing panel mass
$\bar{V}$	frustum volume

[*] Ph.D. Student, AIAA Member
[†] Research Associate Professor, AIAA Member
[‡] Associate Professor, AIAA Senior Member

V^*	reduced velocity, $\frac{U_\infty}{b_s \omega_\alpha}$
V_f	flutter speed index, $\frac{V^*}{\bar{\mu}}$
ω_α	1st torsional mode natural frequency
$\bar{\mu}$	mass ratio, $\frac{\bar{m}}{\bar{V}\rho_\infty}$
ω_j	natural frequency for jth mode
ζ_j	modal damping ratio for jth mode

Abbreviations

$CUSP$	convective upwind and split pressure
DES	detached eddy simulation
$DDES$	delayed detached eddy simulation
FSI	fluid/structure interaction
$WENO$	weighted essentially non-oscillatory

1 Introduction

Flutter is an aeroelastic self-excited instability induced by the fluid structure interaction of deformable structure with surrounding fluid flow. If vibration induced by the aerodynamic force acting on the structure exceeds a condition of dynamic equilibrium, flutter of an aircraft occurs, and often results in the structural failure. Therefore, tools for aerodynamic flutter predictions are key to success in the design of an aircraft.

The governing equations of the flow and the structure need to be simultaneously integrated in time in order to reflect the true fluid-structural interaction. Most of the studies on fluid-structural interaction[1, 2, 3, 4, 5, 6] has been implemented by a staggered or loosely coupled procedure. In this way the information is exchanged after partial or complete convergence of individual solvers with time lag. For example, Liu et al.[4] used a loosely coupled approach for AGARD 445.6 wing flutter calculations. The equations governing the flow and the displacement of the structure are solved separately by two distinct solvers. Deformed grid is obtained by an energy conservative interpolation procedure between two different grid systems.

Alonso and Jameson[7] used a tightly coupled approach for 2D Euler aeroelastic simulations with explicit Runge-Kutta time marching method. At time level n, the pseudo-time calculation is conducted, and the flow information is sent to the structural solver. Then, the new position is taken into account by the flow solver which repeats the process. The two systems exchange information after every pseudo-time step. In general, about 100 pseudo-time steps are needed for the explicit schemes to ensure adequate convergence[3, 4]. Yang et al.[8] also presented an implicit coupled fluid-structure coupling based on the Runge-Kutta time integration scheme. The combined systems of fluid and structural equations are solved in a strongly coupled manner to eliminate time lag between the flow and the structure solution at each physical time step.

Chen et al.[9, 10] conducted a fully coupled fluid-structural interaction simulation to predict the AGARD wing flutter boundary. In their study, time accurate Navier-Stokes equations are solved with a system of N-decoupled structure modal equations in a fully coupled manner. To decouple the equation of motion, transformation of the structural equations to the modal coordinates are applied. The flow field and structure always respond simultaneously by exchanging the unsteady aerodynamic force and structural displacement within each physical time step via successive iterations on the pseudo-time step. Their approach is adopted in this study. A full convergence with residual reduced by 3-4 order of magnitudes is usually reached with 30 iterations within a physical time step.

Prediction of supersonic flutter is particularly challenging since the flow involves complicated nonlinear phenomena such as shock wave/boundary layer interaction and flow separation. So far, the flutter boundary prediction for AGARD wing can agree with the experimental measurement fairly well at subsonic Mach number including the sonic dip.

However, currently the flutter boundary predictions for AGARD Wing at supersonic incoming flow agree poorly with the experimental measurement. For example, for the AGARD wing 445.6 at Mach number of 1.141, Liu et al.[4] used Jameson's explicit Runge-Kutta scheme and overpredicted the flutter velocity index by 61.74%. Rausch et al.[1] also overpredicted the flutter boundary by about 20% using the upwind flux vector splitting scheme with Baldwin-Lomax turbulence model. Xiao et al.[2] overpredicted the flutter boundary by 34% using a loosely coupled FSI procedure with Menter's $k-\omega$ turbulence model. Yang et al.[8] overpredicted by 58.7% using Baldwin-Lomax turbulence model. Chen et al.[10] overpredicted by 14% using a RANS Baldwin-Lomax model. In general, almost all

the current CFD simulations for supersonic flutter boundary overpredict the flutter boundary with a large discrepency.

Turbulence simulation is critical for simulating shock/boundary layer interaction at supersonic aeroelasticity problems. All the aforementioned fluid-structural interaction studies are based on Reynolds-averaged Navier-Stokes equations. However, RANS methods intend to model the large scale eddies using a universal model. Large scale turbulence is affected by the flow geometry and boundary conditions and a universal model does not exist.

Large Eddy Simulation (LES) is promising to overcome the disadvantages of the RANS model. In LES, the governing equations are spatially filtered on the scale of the numerical grid. The large energy containing scales are directly simulated, and the small scale eddies, which are generally more homogeneous and universal, are modeled. The large eddies are strongly affected by the flow field geometry boundaries. Therefore the direct computation of the large eddies by LES is more accurate than modeling of the large eddies by RANS. However, for high Reynolds number flows such as those of transonic wings and turbomachinery blades, to resolve wall boundary layer, LES needs the CPU resource not much less than the Direct Numerical Simulation(DNS). This makes the LES too expensive for fluid-structural interaction unsteady calculations. For engineering applications, it is not hopeful for LES to be rigorously used until in another 4 decades[11].

To overcome the intensive CPU requirement for LES, Spalart et al. developed the detached eddy simulation (DES) strategy[11], which is a hybrid RANS and LES method. Near the solid surface within the wall boundary layer, the unsteady RANS model is realized. Away from the wall surface, the model automatically converts to LES. By using the RANS model near walls, the mesh size as well as the CPU time can be tremendously reduced. The motivation of DES is that the LES is powerful in regions of massive separation and other free shear flows such as jets, but much too costly in the large area of thin wall boundary layers.

Spalart et al.[12] suggest a delayed DES (DDES) in 2006 to overcome the modeled stress depletion (MSD) problem of the original DES when the mesh is thin compared with boundary layer thickness. With DDES, a blending function similar to the one used by Menter and Kuntz[13] for the SST model is introduced to limit the length scale of DES97 to ensure the transition of RANS to LES be independent of grid spacing.

Even though DES concept is much newer than RANS and LES concept, its application for turbulence simulation has achieved encouraging success. Wang and Zha[14] simulate a co-flow jet airfoil using DES at high angle of attack with the results significantly improved compared with that obtained by RANS. Furthermore, Wang and Zha[15] apply the DES to fluid-structural interaction and accurately predict the limited cycle oscillation amplitude and frequency. Im and Zha [16] use DDES and accurately simulate a massive separation flow of NACA0012 airfoil. DDES appears to be a suitable compromise between the physical models of turbulence and CPU efficiency.

The purpose of this paper is to simulate the challenging supersonic AGARD wing flutter boundary using a high fidelity DDES[12] with a fully coupled FSI. To our knowledge, no DDES has ever been used for fluid-structural interaction. The 5th order WENO scheme for the inviscid flux and the 4th order central differencing for the viscous flux are used with the Low Diffusion E-CUSP (LDE) Scheme to resolve nonlinear shock wave/turbulent boundary layer interaction of the vibrating wing. An efficient spring mesh system is implemented for mesh deformation. The high-scalability parallel computing is applied to save wall clock time[17]. The supersonic flutter boundary predicted is in excellent agreement with the experiment. This appears to be the first time that a numerical simulation matches the experimental supersonic flutter boundary accurately.

2 Numerical Model for Fluid Flow

2.1 Navier-Stokes Equations

The spatially filtered unsteady compressible Navier-Stokes equations governing the viscous flow over the 3D wing can be written in a normalized form in the generalized coordinates(ξ, η, ζ).

$$\frac{\partial \mathbf{Q}}{\partial t} + \frac{\partial \mathbf{E}}{\partial \xi} + \frac{\partial \mathbf{F}}{\partial \eta} + \frac{\partial \mathbf{G}}{\partial \zeta} = \frac{1}{Re}\left(\frac{\partial \mathbf{E}_v}{\partial \xi} + \frac{\partial \mathbf{F}_v}{\partial \eta} + \frac{\partial \mathbf{G}_v}{\partial \zeta}\right) \tag{1}$$

where Re is the Reynolds number. The equations are nondimenisonalized based on airfoil chord L_∞, freestream density ρ_∞, velocity U_∞, and viscosity μ_∞. The conservative variable vector $\mathbf{Q}$, the inviscid flux vectors $\mathbf{E}$, $\mathbf{F}$, $\mathbf{G}$, and the viscous flux $\mathbf{E_v}$, $\mathbf{F_v}$, $\mathbf{G_v}$ are expressed as

$$\mathbf{Q}=\frac{1}{J}\begin{pmatrix}\bar{\rho}\\ \bar{\rho}\tilde{u}\\ \bar{\rho}\tilde{v}\\ \bar{\rho}\tilde{w}\\ \bar{\rho}\tilde{e}\end{pmatrix},\mathbf{E}=\begin{pmatrix}\bar{\rho}U\\ \bar{\rho}\tilde{u}U+l_x\bar{p}\\ \bar{\rho}\tilde{v}U+l_y\bar{p}\\ \bar{\rho}\tilde{w}U+l_z\bar{p}\\ (\bar{\rho}\tilde{e}+\bar{p})\,U-l_t\bar{p}\end{pmatrix},\mathbf{F}=\begin{pmatrix}\bar{\rho}V\\ \bar{\rho}\tilde{u}V+m_x\bar{p}\\ \bar{\rho}\tilde{v}V+m_y\bar{p}\\ \bar{\rho}\tilde{w}V+m_z\bar{p}\\ (\bar{\rho}\tilde{e}+\bar{p})\,V-m_t\bar{p}\end{pmatrix},\mathbf{G}=\begin{pmatrix}\bar{\rho}W\\ \bar{\rho}\tilde{u}W+n_x\bar{p}\\ \bar{\rho}\tilde{v}W+n_y\bar{p}\\ \bar{\rho}\tilde{w}W+n_z\bar{p}\\ (\bar{\rho}\tilde{e}+\bar{p})\,W-n_t\bar{p}\end{pmatrix} \tag{2}$$

$$\mathbf{E_v}=\begin{pmatrix}0\\ l_k\bar{\tau}_{xk}\\ l_k\bar{\tau}_{yk}\\ l_k\bar{\tau}_{zk}\\ l_k\left(\tilde{u}_i\bar{\tau}_{ki}-\bar{q}_k\right)\end{pmatrix},\mathbf{F_v}=\begin{pmatrix}0\\ m_k\bar{\tau}u_{xk}\\ m_k\bar{\tau}_{yk}\\ m_k\bar{\tau}u_{zk}\\ m_k\left(\tilde{u}_i\bar{\tau}_{ki}-\bar{q}_k\right)\end{pmatrix},\mathbf{G_v}=\begin{pmatrix}0\\ n_k\bar{\tau}_{xk}\\ n_k\bar{\tau}_{yk}\\ n_k\bar{\tau}_{zk}\\ n_k\left(\tilde{u}_i\bar{\tau}_{ki}-\bar{q}_k\right)\end{pmatrix} \tag{3}$$

where ρ is the density, p is the static pressure, and e is the total energy per unit mass. The overbar denotes a regular filtered variable, and the tilde is used to denote the Favre filtered variable, ν is kinematic viscosity and $\tilde{\nu}$ is the working variable related to eddy viscosity in DDES model. U, V and W are the contravariant velocities in ξ, η, ζ directions, and are defined as

$$U=l_t+\mathbf{l}\bullet\mathbf{V}=l_t+l_x\tilde{u}+l_y\tilde{v}+l_z\tilde{w} \tag{4}$$

$$V=m_t+\mathbf{m}\bullet\mathbf{V}=m_t+m_x\tilde{u}+m_y\tilde{v}+m_z\tilde{w} \tag{5}$$

$$W=n_t+\mathbf{n}\bullet\mathbf{V}=n_t+n_x\tilde{u}+n_y\tilde{v}+n_z\tilde{w} \tag{6}$$

where J is the Jacobian of the coordinate transformation. l_t, m_t and n_t are the components of the interface contravariant velocity of the control volume in ξ, η and ζ directions respectively. $\mathbf{l}$, $\mathbf{m}$ and $\mathbf{n}$ denote the normal vectors located at the centers of ξ, η and ζ interfaces of the control volume with their magnitudes equal to the surface areas and pointing to the directions of increasing ξ, η and ζ.

$$\mathbf{l}=\frac{\nabla\xi}{J},\ \mathbf{m}=\frac{\nabla\eta}{J},\ \mathbf{n}=\frac{\nabla\zeta}{J} \tag{7}$$

$$l_t=\frac{\xi_t}{J},\ m_t=\frac{\eta_t}{J},\ n_t=\frac{\zeta_t}{J} \tag{8}$$

Let the subscripts i,j,k represent the coordinates x,y,z and use the Einstein summation convention. By introducing the concept of eddy viscosity and sug-grid stress of LES to close the system of equations, the shear stress $\bar{\tau}_{ik}$ and total heat flux $\bar{q}_k$ in Cartesian coordinates can be expressed in tensor form as

$$\bar{\tau}_{ik}=(\mu+\mu_{DES})\left[\left(\frac{\partial\tilde{u}_i}{\partial x_k}+\frac{\partial\tilde{u}_k}{\partial x_i}\right)-\frac{2}{3}\delta_{ik}\frac{\partial\tilde{u}_j}{\partial x_j}\right] \tag{9}$$

$$\bar{q}_k=-\left(\frac{\mu}{Pr}+\frac{\mu_{DES}}{Pr_t}\right)\frac{\partial\tilde{T}}{\partial x_k} \tag{10}$$

where the molecular viscosity $\mu=\mu(\tilde{T})$ is determined by Sutherland's law, and $\mu_{DES}(=\bar{\rho}\tilde{\nu}f_{v1})$ is determined by the DDES of turbulence[12] as explained in the following section. Eq.(9) and (10) are transformed to the generalized coordinate system in computation. The equation of state as a constitutive equation relating density to pressure and temperature is given as follows;

$$\bar{\rho}\tilde{e}=\frac{\bar{p}}{(\gamma-1)}+\frac{1}{2}\bar{\rho}(\tilde{u}^2+\tilde{v}^2+\tilde{w}^2) \tag{11}$$

For simplicity, all the bar and tilde in above equations will be dropped in the rest of this paper.

2.2 Delayed Detached Eddy Simulation of Turbulence[12]

In 2006 Spalart et al.[12] suggested an advanced hybrid RANS/LES turbulence, the delayed detached eddy simulation based on the Spalart-Allmaras one equation model[18] which solves a transport equation for the working variable $\tilde{\nu}$. The turbulent eddy viscosity μ_{DES} related to working variable $\tilde{\nu}$ is given by

$$\mu_{DES} = \rho\nu_t = \rho\tilde{\nu}f_{v1} \tag{12}$$

where

$$f_{v1} = \frac{\chi^3}{\chi^3 + c_{v1}^3} \tag{13}$$

$$\chi = \frac{\tilde{\nu}}{\nu} \tag{14}$$

In the DDES model, the transport equation for the working variable $\tilde{\nu}$ yields in generalized coordinate system as

$$\begin{aligned}\frac{\partial \frac{1}{J}\rho\tilde{\nu}}{\partial t} + \frac{\partial \rho\tilde{\nu}U}{\partial \xi} + \frac{\partial \rho\tilde{\nu}V}{\partial \eta} + \frac{\partial \rho\tilde{\nu}W}{\partial \zeta} = \frac{1}{Re}\left(\frac{\partial \frac{\rho}{\sigma}(\nu+\tilde{\nu})(\mathbf{l}\bullet\nabla\tilde{\nu})}{\partial \xi}\right.\\ \left.+\frac{\partial \frac{\rho}{\sigma}(\nu+\tilde{\nu})(\mathbf{m}\bullet\nabla\tilde{\nu})}{\partial \eta} + \frac{\partial \frac{\rho}{\sigma}(\nu+\tilde{\nu})(\mathbf{n}\bullet\nabla\tilde{\nu})}{\partial \zeta} + \frac{1}{J}S_\nu\right)\end{aligned} \tag{15}$$

where

$$\begin{aligned}S_\nu = \rho c_{b1}(1-f_{t2})\tilde{S}\tilde{\nu} + \frac{1}{Re}\left[-\rho\left(c_{w1}f_w - \frac{c_{b1}}{\kappa^2}f_{t2}\right)\left(\frac{\tilde{\nu}}{d}\right)^2\right.\\ \left.+\frac{\rho}{\sigma}c_{b2}(\nabla\tilde{\nu})^2 - \frac{1}{\sigma}(\nu+\tilde{\nu})\nabla\tilde{\nu}\bullet\nabla\rho\right] + Re\left[\rho f_{t1}(\Delta q)^2\right]\end{aligned} \tag{16}$$

$$\tilde{S} = S + \frac{\tilde{\nu}}{Rek^2d^2}f_{v2} \tag{17}$$

$$f_{v2} = 1 - \frac{\chi}{1+\chi f_{v1}} \tag{18}$$

$$S = \sqrt{2\Omega_{ij}\Omega_{ij}} \tag{19}$$

$$f_w = g\left(\frac{1+c_{w3}^6}{g^6+c_{w3}^6}\right)^{1/6} \tag{20}$$

$$g = r + c_{w2}(r^6 - r) \tag{21}$$

$$r = \frac{\tilde{\nu}}{Re\tilde{S}k^2d^2} \tag{22}$$

$$f_{t2} = c_{t3}exp\left(-c_{t4}\chi^2\right) \tag{23}$$

$$f_{t1} = c_{t1}g_t exp\left[-c_{t2}\frac{\omega_t^2}{\Delta U^2}\left(d^2 + g_t^2 d_t^2\right)\right] \tag{24}$$

$$g_t = min\left(0.1, \frac{\Delta q}{\omega_t \Delta x_t}\right) \tag{25}$$

Where $\Omega_{ij} = \frac{1}{2}\left(\frac{\partial u_i}{\partial x_j} - \frac{\partial u_j}{\partial x_i}\right)$ is the rotation tensor. ω_t is the wall vorticity at the wall boundary layer trip location, d is the distance to the closest wall, d_t is the distance of the field point to the trip location, Δq is the difference of the velocities between the field point and the trip location, Δx_t is the grid spacing along the wall at the trip location. The values of the coefficients by reference[18] are: $c_{b1} = 0.1355, c_{b2} = 0.622, \sigma = \frac{2}{3}, c_{w1} = \frac{c_{b1}}{k^2} + (1+c_{b2})/\sigma, c_{w2} = 0.3, c_{w3} = 2, k = 0.41, c_{v1} = 7.1, c_{t1} = 1.0, c_{t2} = 2.0, c_{t3} = 1.1, c_{t4} = 2.0$.

To overcome the modeled stress depletion (MSD) and avoid grid induced separation in DES97[11], the DDES suggested by Spalart et al.[12] switches the subgrid scale formulation in DES model by redefining the distance to the nearest wall $\tilde{d}$ as

$$\tilde{d} = d - f_d max(0, d - C_{DES}\Delta) \tag{26}$$

where

$$f_d = 1 - tanh([8r_d]^3) \tag{27}$$

$$r_d = \frac{\nu_t + \nu}{(U_{i,j}U_{i,j})^{0.5}k^2d^2Re} \tag{28}$$

$$U_{i,j} = \frac{\partial u_i}{\partial x_j} \tag{29}$$

where $U_{i,j}$ is the velocity gradients, k is the Karman constant, and d is the distance to the nearest wall. Within the boundary layer close to walls, $\tilde{d} = d$, and away from the boundary layer, $\tilde{d} = C_{DES}\Delta$ is most of the cases. f_d is designed to be 1 in the LES region, where $r_d \ll 1$, and 0 elsewhere. Unlike DES97, this modification can fully preserve RANS mode inside boundary layer, therefore attached boundary layers are safe from MSD. This mechanism enables DDES to behave as a RANS model in the near-wall regions, and LES away from the wall.

2.3 The Low Diffusion E-CUSP Scheme for Inviscid Flux

The Low Diffusion E-CUSP(LDE) Scheme[19, 20] is used to evaluate the inviscid fluxes. The basic idea of the LDE scheme is to split the inviscid flux into the convective flux E^c and the pressure flux E^p based on the upwind characteristics. With an extra equation from the DDES model, the splitting is basically the same as the original scheme for the Euler equation. This is an advantage over the Roe scheme[21], for which the eigenvectors need to be derived when any extra equation is added to the governing equations. In generalized coordinate system, the flux $\mathbf{E}$ can be split as the following:

$$\mathbf{E}' = E^c + E^p = \begin{pmatrix} \rho U \\ \rho u U \\ \rho v U \\ \rho w U \\ \rho e U \\ \rho \tilde{\nu} U \end{pmatrix} + \begin{pmatrix} 0 \\ l_x p \\ l_y p \\ l_z p \\ p\overline{U} \\ 0 \end{pmatrix} \tag{30}$$

where, U is the contravariant velocity in ξ direction and is defined as the following:

$$U = l_t + l_x u + l_y v + l_z w \tag{31}$$

$\overline{U}$ is defined as:

$$\overline{U} = l_x u + l_y v + l_z w \tag{32}$$

The convective term, E^c is evaluated by

$$E^c = \rho U \begin{pmatrix} 1 \\ u \\ v \\ w \\ e \\ \tilde{\nu} \end{pmatrix} = \rho U f^c,\ f^c = \begin{pmatrix} 1 \\ u \\ v \\ w \\ e \\ \tilde{\nu} \end{pmatrix} \tag{33}$$

let

$$C = c\left(l_x^2 + l_y^2 + l_z^2\right)^{\frac{1}{2}} \tag{34}$$

where $c = \sqrt{\gamma RT}$ is the speed of sound.

Then the convective flux at interface $i + \frac{1}{2}$ is evaluated as:

$$E^c_{i+\frac{1}{2}} = C_{\frac{1}{2}}\left[\rho_L C^+ f^c_L + \rho_R C^- f^c_R\right] \tag{35}$$

where, the subscripts L and R represent the left and right hand sides of the interface. The Mach number splitting of Edwards[22] is borrowed to determine c^+ and c^- as the following:

$$C_{\frac{1}{2}} = \frac{1}{2}\left(C_L + C_R\right) \tag{36}$$

$$C^+ = \alpha_L^+ \left(1 + \beta_L\right) M_L - \beta_L M_L^+ - M_{\frac{1}{2}}^+ \tag{37}$$

$$C^- = \alpha_R^- \left(1 + \beta_R\right) M_R - \beta_R M_R^- + M_{\frac{1}{2}}^- \tag{38}$$

$$M_L = \frac{U_L}{C_{\frac{1}{2}}},\ M_R = \frac{U_R}{C_{\frac{1}{2}}} \tag{39}$$

$$\alpha_{L,R} = \frac{1}{2}\left[1 \pm sign\left(M_{L,R}\right)\right] \tag{40}$$

$$\beta_{L,R} = -max\left[0, 1 - int\left(\left|M_{L,R}\right|\right)\right] \tag{41}$$

$$M_{\frac{1}{2}}^+ = M_{\frac{1}{2}} \frac{C_R + C_L\Phi}{C_R + C_L},\ M_{\frac{1}{2}}^- = M_{\frac{1}{2}} \frac{C_L + C_R\Phi^{-1}}{C_R + C_L} \tag{42}$$

$$\Phi = \frac{\left(\rho C^2\right)_R}{\left(\rho C^2\right)_L} \tag{43}$$

$$M_{\frac{1}{2}} = \beta_L \delta^+ M_L^- - \beta_R \delta^- M_R^+ \tag{44}$$

$$M_{L,R}^{\pm} = \pm\frac{1}{4}\left(M_{L,R} \pm 1\right)^2 \tag{45}$$

$$\delta^{\pm} = \frac{1}{2}\left\{1 \pm sign\left[\frac{1}{2}\left(M_L + M_R\right)\right]\right\} \tag{46}$$

The pressure flux, E^p is evaluated as the following

$$E_{i+\frac{1}{2}}^p = \begin{pmatrix} 0 \\ \mathcal{P}^+ p\, l_x \\ \mathcal{P}^+ p\, l_y \\ \mathcal{P}^+ p\, l_z \\ \frac{1}{2} p\left[\overline{U} + \overline{C}_{\frac{1}{2}}\right] \\ 0 \end{pmatrix}_L + \begin{pmatrix} 0 \\ \mathcal{P}^- p\, l_x \\ \mathcal{P}^- p\, l_y \\ \mathcal{P}^- p\, l_z \\ \frac{1}{2} p\left[\overline{U} - \overline{C}_{\frac{1}{2}}\right] \\ 0 \end{pmatrix}_R \tag{47}$$

The contravariant speed of sound $\overline{C}$ in the pressure vector is consistent with $\overline{U}$. It is computed based on C as the following,

$$\overline{C} = C - l_t \tag{48}$$

The use of $\overline{U}$ and $\overline{C}$ instead of U and C in the pressure vector is to take into account of the grid speed so that the flux will transit from subsonic to supersonic smoothly. When the grid is stationary, $l_t = 0$, $\overline{C} = C$, $\overline{U} = U$.

The pressure splitting coefficient is:

$$\mathcal{P}_{L,R}^{\pm} = \frac{1}{4}\left(M_{L,R} \pm 1\right)^2 \left(2 \mp M_L\right) \tag{49}$$

The LDE scheme can capture crisp shock profile and exact contact surface discontinuities as accurately as the Roe scheme[20]. However, it is simpler and more CPU efficient than the Roe scheme due to no matrix operation. In the reference[23], the LDE scheme is shown to be more efficient than the Roe scheme when the S-A one equation turbulence model is coupled.

2.4 The 5th Order WENO Scheme

For reconstruction of the interface flux, $E_{i+\frac{1}{2}} = E(Q_L, Q_R)$, the conservative variables Q_L and Q_R are evaluated by using the 5th order WENO scheme[24, 25]. For example,

$$(Q_L)_{i+\frac{1}{2}} = \omega_0 q_0 + \omega_1 q_1 + \omega_2 q_2 \tag{50}$$

where

$$q_0 = \frac{1}{3}Q_{i-2} - \frac{7}{6}Q_{i-1} + \frac{11}{6}Q_i \tag{51}$$

$$q_1 = -\frac{1}{6}Q_{i-1} + \frac{5}{6}Q_i + \frac{1}{3}Q_{i+1} \tag{52}$$

$$q_2 = \frac{1}{3}Q_i + \frac{5}{6}Q_{i+1} - \frac{1}{6}Q_{i+2} \tag{53}$$

$$\omega_k = \frac{\alpha_k}{\alpha_0 + \ldots + \alpha_{r-1}} \tag{54}$$

$$\alpha_k = \frac{C_k}{\epsilon + IS_k},\ k = 0, \ldots, r-1 \tag{55}$$

$$C_0 = 0.1,\ C_1 = 0.6,\ C_2 = 0.3 \tag{56}$$

$$IS_0 = \frac{13}{12}\left(Q_{i-2} - 2Q_{i-1} + Q_i\right)^2 + \frac{1}{4}\left(Q_{i-2} - 4Q_{i-1} + 3Q_i\right)^2 \tag{57}$$

$$IS_1 = \frac{13}{12}\left(Q_{i-1} - 2Q_i + Q_{i+1}\right)^2 + \frac{1}{4}\left(Q_{i-1} - Q_{i+1}\right)^2 \tag{58}$$

$$IS_2 = \frac{13}{12}\left(Q_i - 2Q_{i+1} + Q_{i+2}\right)^2 + \frac{1}{4}\left(3Q_i - 4Q_{i+1} + Q_{i+2}\right)^2 \tag{59}$$

ϵ is originally introduced to avoid the denominator becoming zero and is supposed to be a very small number. In the reference[25, 26], it is observed that IS_k will oscillate if ϵ is too small and also shift the weights away from the optimal values in the smooth region. The higher the ϵ values, the closer the weights approach the optimal values, C_k, which will give the symmetric evaluation of the interface flux with minimum numerical dissipation. When there are shocks in the flow field, ϵ can not be too large to maintain the sensitivity to shocks. In reference[25, 26], $\epsilon = 10^{-2}$ is recommended for the transonic flow with shock waves.

2.5 Time Marching Scheme

The time dependent governing equation (1) is solved using dual time stepping method suggested by Jameson[27]. A pseudo temporal term $\frac{\partial Q}{\partial \tau}$ is added to the governing Eq. (1). This term vanishes at the end of each physical time step, and has no influence on the accuracy of the solution. An implicit pseudo time marching scheme using Gauss-Seidel line relaxation is employed to achieve high convergence rate instead of using the explicit scheme[26]. The pseudo temporal term is discretized with first order Euler scheme. Let m stand for the iteration index within a physical time step, the semi-discretized governing equation can be expressed as

$$\begin{aligned}\left[\left(\tfrac{1}{\Delta\tau} + \tfrac{1.5}{\Delta t}\right) I - \left(\tfrac{\partial R}{\partial \mathbf{Q}}\right)^{n+1,m}\right] \delta\mathbf{Q^{n+1,m+1}} \\ = R^{n+1,m} - \tfrac{3\mathbf{Q^{n+1,m}} - 4\mathbf{Q^{n}} + \mathbf{Q^{n-1}}}{2\Delta t}\end{aligned} \tag{60}$$

where $\Delta\tau$ is the pseudo time step, and R is the net flux of the Navier-Stokes equations discretized in space using the schemes described in section II. C to II. D.

3 Structural Model

3.1 Modal Approach

The equation of motion of an N-DOF(degree of freedom) system with mechanical damping and the aerodynamic loading as the excitation force can be presented in matrix form:

$$[\mathbf{M}]\{\ddot{\mathbf{X}}\} + [\mathbf{C}]\{\dot{\mathbf{X}}\} + [\mathbf{K}]\{\mathbf{X}\} = \{\mathbf{F}\} \tag{61}$$

where, **M**, **C**, **K** are the mass, structural damping and stiffness matrices. **F** is total aerodynamic force acting on the wing surface. Total aerodynamic force can be defined as follows:

$$\mathbf{F} = -\oint P \cdot \hat{n} dA + \oint \tau_{\mathbf{w}} \cdot \hat{t} dA \tag{62}$$

where, $\hat{n}$ is the unit normal vector to the wing surface and $\hat{t}$ is the unit tangent vector to the wing surface. P is the fluid static pressure and $\tau_{\mathbf{w}}$ is the fluid wall shear stress acting on the wing surface. Eq. (11) is used to compute static pressure of the wing surface by setting flow velocity components to zero.

To decouple the equations of motion for the damped systems(61), we use the mass normalized mode shape($\tilde{\phi}$) defined as the normal modes divided by square root of the generalized mass($\sqrt{\phi^T m \phi}$). Let $\{\mathbf{X}\} = [\tilde{\Phi}]\{\mathbf{q}\}$ and premultiply Eq. (61) by the transpose $[\tilde{\Phi}]^T$.

$$\begin{aligned}[\tilde{\Phi}]^T[\mathbf{M}][\tilde{\Phi}]\{\ddot{\mathbf{q}}\} + [\tilde{\Phi}]^T[\mathbf{C}][\tilde{\Phi}]\{\dot{\mathbf{q}}\} + [\tilde{\Phi}]^T[\mathbf{K}][\tilde{\Phi}]\{\mathbf{q}\} \\ = [\tilde{\Phi}]^T\{\mathbf{F}\}\end{aligned} \tag{63}$$

where **q** is the vector of the principal coordinates. Using the orthogonality of the system matrices and assuming damping matrix to be a linear combination of the mass and stiffness matrices, Eq. (63) is then completely decoupled and the jth equation will have the form

$$\ddot{q}_j + 2\zeta_j \omega_j \dot{q}_j + \omega_j^2 q_j = \frac{\tilde{\phi}_j^T}{m_j}\mathbf{F} \tag{64}$$

where $[\tilde{\Phi}]^T = [\tilde{\phi}_1, \cdots, \tilde{\phi}, \cdots, \tilde{\phi}_N]^T$. N is the number of modal coordinates. ω_j and ζ_j are natural frequency and modal damping ratio for mode j. m_j denotes the jth diagonal element of modal mass matrix that is unity. In the current study, the structural system may be reduced to only five mode shapes, since a few bending and torsional frequencies are usually sufficient to determine flutter. The normalized modal equation can be given as[10]

$$\ddot{q}_j + 2\zeta_j(\tfrac{\omega_j}{\omega_\alpha})\dot{q}_j + (\tfrac{\omega_j}{\omega_\alpha})^2 q_j = \frac{\tilde{\phi}_j^{*T}}{m_j^*} \cdot \mathbf{F}^* \cdot {V_f}^2 \cdot \frac{b_s^2 L}{\bar{V}} \cdot \bar{m} \tag{65}$$

where the dimensionless quantities are denoted by an asterisk. $V_f(= \frac{U_\infty}{b_s \omega_\alpha \sqrt{\bar{\mu}}})$ is the flutter speed index which is an input flutter control parameter. $\bar{m}$ is the measure wing panel mass, $\bar{V}$ represents the conical frustum volume and b_s is the streamwise root semi chord. L is the reference length and ω_α is the angular frequency of the first torsional mode in units of *radians/sec*. $\bar{\mu}(= \frac{\bar{m}}{\bar{V}\rho_\infty})$ stands for the mass ratio, i.e. the ratio between the structural mass and the mass of the equivalent volume of fluid at reference density. It is noticed that m_j^* should be equal to one when the mass normalized mode shapes are used. For example, the mode shapes of AGARD wing 445.6 Weakend model 3 reported by Yates[28] are normalized using the generalized mass such that m_j^* equals one in units $lbf \cdot in \cdot s^2$. This corresponds to 0.112979 $kg \cdot m^2$ in SI units.

The structure equations are then transformed to a state form as follows:

$$[\mathbf{M}]\frac{\partial \mathbf{S}}{\partial t} + [\mathbf{K}]\{\mathbf{S}\} = \mathbf{q} \tag{66}$$

where

$$\mathbf{S} = \begin{pmatrix} q_j \\ \dot{q}_j \end{pmatrix}, \mathbf{M} = [I], \mathbf{K} = \begin{pmatrix} 0 & -1 \\ (\frac{\omega_j}{\omega_\alpha})^2 & 2\zeta_j(\frac{\omega_j}{\omega_\alpha}) \end{pmatrix}$$

$$\mathbf{q} = \begin{pmatrix} 0 \\ \phi_j^{*T} \cdot \mathbf{F}^* \cdot V_f \cdot \frac{b_s^2 L}{\bar{V}} \cdot \bar{m} \end{pmatrix}$$

3.2 Implicit Structural Solver

To solve the structural equations with CFD solver[19, 20] in a fully coupled manner[10], the decoupled structural equations are integrated using the same method as the flow governing equations(60) within each physical time step:

$$\begin{aligned}&\left(\tfrac{1}{\Delta\tau}I+\tfrac{1.5}{\Delta t}M+K\right)\delta S^{n+1,m+1}\\&=q^{n+1,m+1}-M\tfrac{3S^{n+1,m}-4S^{n}+S^{n-1}}{2\Delta t}-KS^{n+1,m}\end{aligned}\tag{67}$$

Within each physical time step, the flow equations and structural equations are solved iteratively via every successive pseudo time step until the prescribed convergence criteria is satisfied for both flow and structural solver. After the convergence criteria is reached, the fluid-structural interaction goes to next physical time step.

3.3 Moving Mesh

A CPU efficient deformation mesh technique is one of the requisites in FSI to accurately describe a moving structure. An algebraic deformation mesh technique for the 3D wing is implemented by using the spring mesh algorithm suggested by Chen et al.[10]. The algorithm is tested for a 2D airfoil with sharp trailing edge as shown in Fig. 1. This moving mesh method works robustly for large deformation. Once the moving mesh for a 2D wing section is generated, the 3D mesh is generated straightforwardly by stacking each airfoil section from the root to tip due to the small deformation in the spanwise direction. Note that an important factor affecting the deformed mesh quality is the initial mesh skewness, in particular near the wing surface. Therefore, the O-mesh topology is used in this study to maintain the mesh orthogonality near the wing surface.

4 Boundary Conditions

For the subsonic flutter calculations, steady state freestream conditions are used at the upstream portion of the outer boundary. At downstream boundary, the static pressure is specified as freestream value, and the streamwise gradients of other variables are forced to vanish. In spanwise direction, the periodic boundary condition is used. For the supersonic flutter case, all the variables are extrapolated at downstream boundary. The supersonic inflow condition with all variables specified is applied at the upstream portion of the outer boundary. The rest of the boundary conditions for the supersonic case are the same as those for the subsonic cases. The wall treatment suggested in [25, 26] to achieve flux conservation by shifting half interval of the mesh on the wall is employed.

5 Parameters for Flutter Control

There are in general three wing flutter control(or input) parameters: mass ratio $\bar{\mu}=\frac{\bar{m}}{\bar{V}\rho_\infty}$, reduced velocity $V^*=\frac{U_\infty}{b_s\omega_\alpha}$, and flutter speed index $V_f=\frac{V^*}{\bar{\mu}}$. The mass ratio $\bar{\mu}$ takes into account the effect of stiffness in flutter. It represents the ratio between the structural mass and the mass of the equivalent volume of fluid at reference density. Typically flutter speed index V_f is selected as the main parameter in flutter boundary prediction because V_f reflects the effects of both dynamic pressure of the surrounding flow and stiffness of the structure. The effect of aircraft altitude in wind tunnel tests[28, 29] is obtained based on variation of dynamic pressure(varying the density) at constant Mach number. Liu[4] and Chen[10] used V_f, whereas Bakhle[30] used V^* to find the flutter boundary at a given Mach number. In this study, either V_f or V^* can be used explicitly as shown in Eq. (65). The V_f is selected for the wing flutter simulation.

Several iterations are usually needed for a given freestream Mach number to search the neutrally stable point, which is treated as the flutter boundary. Most of the computations only need to calculate a few periods to see whether the responses are divergent or damped with time. The flutter velocity index V_f is iterated to find the flutter boundary, all other variables such as inlet total pressure, inlet total temperature, and the static pressure at outlet are not varied. The Reynolds number, $R_e=\frac{\rho_\infty U_\infty L_\infty}{\mu_\infty}$ varies with the freestream velocity. In the wing flutter experiment[29], dynamic pressure $q=\frac{1}{2}\rho_\infty V_\infty^2$ is the main fluid quantity to adjust flutter level. The way to control the dynamic pressure is either by varying the free stream density using the real gas such as freon-12 or by changing the velocity instead of density. In this paper, we vary the freestream velocity, U_∞, which has direct relation with the reduced velocity V^*, and hence the flutter velocity index V_f.

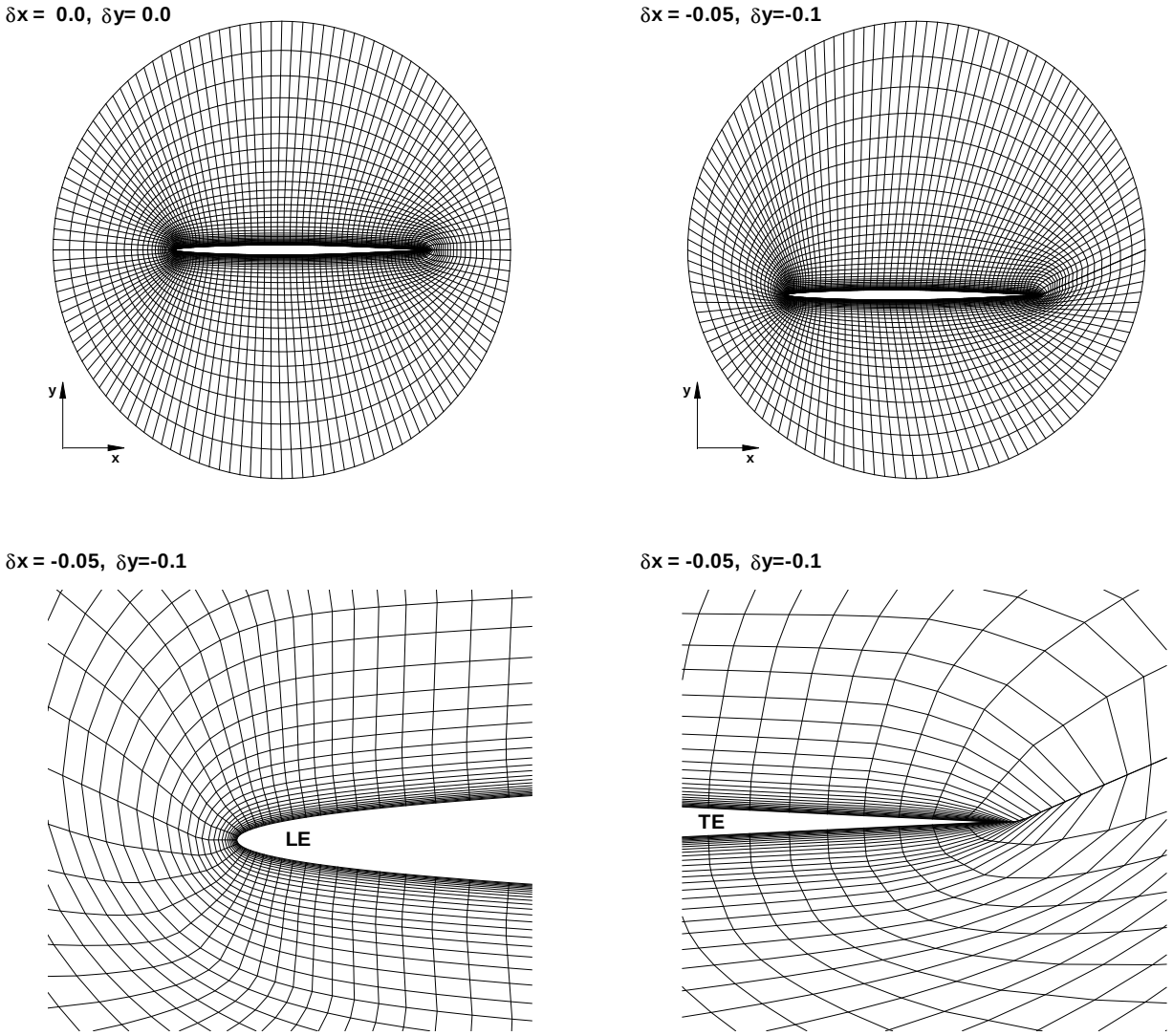

Figure 1: Moving mesh test for an airfoil; initial mesh(top left), deformed mesh by $\delta x = -0.05, \delta y = -0.1$(top right), magnified view of deformed mesh near leading edge(bottom left), magnified view of deformed mesh near trailing edge(bottom left)

6 AGARD Wing 445.6 Model

A limited number of AGARD standard wing configurations were tested[28] in order to promote the evaluation of existing and emerging unsteady aerodynamics codes and methods for flutter from subsonic to supersonic regime. In this study, the AGARD Wing 445.6 Weakend 3 is used for flutter simulation. This wing model has the symmetric NACA65A004 airfoil with a 4% thickness, and the wing structural details are listed in table 1.

7 Results and Discussion

First five mass normalized mode shapes in the report[28] are used, which are displayed in Fig. 2. Those are identified that 1st, 3rd and 5th mode are bending, and 2nd and 4th mode are torsion. As initial conditions for the structure, 1st mode initial velocity of the structure in the modal coordinates is assumed as 0.0001 whereas others including modal displacements are set to zero. The uniform modal damping ratio(ζ) of 0.005 is applied for all flutter computations since no structural damping is available[5]. The physical time step 0.05 with the pseudo time CFL number of 1 is used. Before the flutter computation, the unsteady DDES simulation is conducted for about 2000

Table 1: AGARD Wing 44.5 Weakend 3 model at test Mach number of 1.141[28]

Airfoil section	NACA 65A004
Measured panel mass($\bar{m}$) [kg]	1.8627
Panel span(H) [m]	0.762
Sweep angle at half chord [deg]	43.15
Root chord(b_s) [m]	0.559
Tip chord(b_t) [m]	0.3682
Air density(ρ_∞) [kg/m^3]	0.0783
Dynamic pressure(q) [Pa]	5041.791
Flutter frequency(ω_f) [rads/s]	109.9
Mass ratio($\bar{\mu} = \frac{\bar{m}}{\rho_\infty V}$)	182.74
Flutter index($V_f = \frac{U_\infty}{b_s \omega_f \sqrt{(\bar{\mu})}}$)	0.4031

physical steps to provide initial FSI flow field. The residual in each pseudo time step is required to be reduced by two orders of magnitude, which is achieved usually within 20 iterations.

7.1 Computational Mesh Test

Mesh convergence test is done for Mach number of 0.678. Four mesh sizes were tested; mesh A=137 (around airfoil)×61(normal to the surface)×60(span), mesh B=$137 \times 76 \times 60$, mesh C=$137 \times 91 \times 60$, mesh D=$137 \times 91 \times 70$. When the mesh is changed, the mode shapes corresponding to the surface mesh coordinates are found by a spline interpolation. The 1st grid spacing away from the the wing surface is set to yield y^+ less than unity. The far field boundary is located 50 root chords away from the wing. The O-mesh topology is used as shown in Fig. 3. The outer span boundary from the wing tip is 1 span length of the wing. Total 16 partitioned blocks are used for parallel computation.

Fig. 4 shows the modal displacements of mode 1 and mode 2 for different meshes. The flutter velocity index V_f used for mesh test is 0.415445. The predicted responses for both mode 1 and mode 2 using mesh C are well converged with mesh D. Therefore, mesh C is chosen for flutter simulations in this study.

Fig. 5, and Fig. 6 shows the predicted modal displacements with $V_f = 0.4196$, $V_f = 0.42187$ respectively. It is shown that $V_f = 0.4196$ results in the decaying responses of wing vibration, whereas $V_f = 0.42187$ leads to the neutral responses. Compared with the flutter velocity index of 0.4174 at the stability limit by the experiment[28], the present prediction at Mach number of 0.678 only over-predicts by 0.5%.

7.2 Supersonic Flutter Simulation of AGARD Wing 445.6

The predicted modal displacements for Mach number of 1.141 with different flutter velocity index(V_f) setting are displayed in Fig. 7. At $V_f = 0.3765$, the response decays in time, while $V_f = 0.4304$ leads to divergent responses. A neutrally stable point, the flutter boundary, is captured at $V_f = 0.3993$, which is a harmonic oscillation. The damped oscillation with $V_f = 0.3963$, 0.75% below the measured flutter boundary, indicates that the present FSI approach has good accuracy and is sensitive to a small change of the flutter speed index.

Fig. 8 represents the lift(C_l), the drag(C_d), and the momentum coefficient(C_m) for $V_f = 0.3993$, and $V_f = 0.4304$. At the flutter boundary, all show a type of limited oscillation with same phase angle, period, and amplitude, whereas C_d, C_m with $V_f = 0.4304$ amplifies with time. It is shown that the lift force acting on the wing surface in particular has larger effect due to the flutter than the drag. The momentum coefficient increases too, but its phase is lagged by a half period of oscillation compared to the lift coefficient.

Fig. 9 shows the modal force defined as $\frac{\tilde{\phi}_j^{*T}}{m_j^*} \cdot \mathbf{F}^* \cdot {V_f}^2 \cdot \frac{b_s^2 L}{V} \cdot \bar{m}$ for $V_f = 0.3993$, and $V_f = 0.4304$. For all 5 modes, the modal force also increases with the flutter speed index, $V_f = 0.4304$. It is expected that the wing vibrates mainly in the plunging motion and slightly in the torsional mode since the first mode is bending and the second mode is torsion.

Fig. 10 illustrates how the wing vibrates during the flutter with the flutter velocity of $V_f = 0.4304$. The distance

of the trailing edge is larger than that of the leading edge, which indicates that both the pithing and the plunging are associated with the wing flutter. The wing with the pitching (or torsion) experiences a variation of angle of attack(AOA) with time.

Fig. 11 shows an instantaneous Mach number contours near the tip section during the supersonic flutter. The unsteady shock waves near the trailing edge are well captured. The surface isentropic Mach number at $T = 150$ and $T = 200$ is plotted in Fig. 12. Certainly the difference of the isentropic Mach number is larger near the leading edge due to the variation of the AOA.

Fig. 13 shows an instantaneous Mach number contours of root span, 50% span, tip span at $T = 200$. At root span, the expansion waves are seen near leading and trailing edge, but at 50% span the oblique shocks appear near the trailing edge instead of the expansion waves. The shocks near the trailing edge become stronger toward tip, and the normal shock boundary layer interaction causes a minor flow separation on the pressure surface.

The predicted flutter boundary at a supersonic condition, $M = 1.141$ is presented in Fig. 14. $V_f = 0.3993$ is the flutter velocity index at the flutter boundary resolved in this computation, which is 0.9% lower than the experiment. To our knowledge, the present solution is the first time that a numerical simulation matches the experiment accurately for the supersonic flutter boundary.

8 Conclusion

The supersonic flutter boundary of the 3D AGARD wing is simulated using the delayed detached eddy simulation with a fully coupled fluid/strcuture interaction. The low diffusion E-CUSP scheme with a 5th order WENO reconstruction for the inviscid flux and a set of 4th order central differencing for the viscous terms are used to accurately capture the shock wave/turbulent boundary layer interaction of the vibrating wing. The present simulation at Mach number of 1.141 achieves excellent agreement with the measured data. It appears to be the first time that a numerical prediction of supersonic flutter boundary matches with experiment accurately. The results indicate that the developed DDES methodology with high order shock capturing scheme and fully coupled FSI is robust and accurate.

Acknowledgement

The grants support from AFRL and the industrial partners of GUIde Consortium, 10-AFRL-1024 and 09-GUIDE-1010, are acknowledged.

References

References

[1] E. M. Lee-Rausch, and J.T. Batina, "Calculation of AGARD wing 445.6 flutter using Navier-Stokes aerodynamics." AIAA Paper 1993-3476, August 9-11, 1993.

[2] J. Xiao, and C. Gu, "Wing Flutter Simulations Using an Aeroelastic Solver Based on the Predictor-corrector Scheme," *Proceedings of the Institution of Mechanical Engineers, Part G: Journal of Aerospace Engineering*, vol. 224, pp. 1193–1210, 2009, doi:10.1243/09544100JAERO756.

[3] G. Yang, S. Obayashi, and J. Nakamichi, "Aileron Flutter Calculation for a Supersonic Fuselage-wing Configuration." ICAS 2002 Congress, 2002.

[4] F. Liu, J. Cai, and Y. Zhu, "Calculation of Wing flutter by a Coupled CFD-CSD method." AIAA-2000-0907, 2000.

[5] L. Cavagna, , G. Quaranta, and P. Mantegazzaa, "Application of NavierStokes simulations for aeroelastic stability assessment in transonic regime ," *Journal of Computer and Fluids*, vol. 85, pp. 818–832, 2007, doi:10.1016/j.compstruc.2007.01.005.

[6] Chen P., and Liu. D., "A Harmonic Gradient Method for Unsteady Supersonic Flow Calculations," *Journal of Aircraft*, vol. 22, pp. 371–379, 1985, doi: 10.2514/3.45134.

[7] J.J. Alonso, and A. Jameson, "Fully-Implicit Time Maraching Aeroelastic Solutions." AIAA Paper 94-0056, 1994.

[8] Z. Yang, and D.J. Mavriplis, "Higher-order Time Integration Schemes for Aeroelastic Applications on Unstructured Meshes." 44th AIAA Aerospace Science Meeting, AIAA, Washington, DC, January 2006, 2006.

[9] X.Y. Chen, and G.-C. Zha, "Fully Coupled Fluid-Structural Interactions Using an Efficient High Solution Upwind Scheme," *Journal of Fluid and Structure*, vol. 20, pp. 1105–1125, 2005, doi:10.1016/j.jfluidstructs.2005.02.011.

[10] X.Y. Chen, G.-C. Zha, M.-T. Yang, "Numerical Simulation of 3-D Wing Flutter with Fully Coupled Fluid-Structural Interaction," *Journal of Computers & Fluids*, vol. 36, pp. 856–867, 2007, doi:10.1016/j.compfluid.2006.08.005.

[11] P.R. Spalart, W.H. Jou, M. Strelets, and S.R. Allmaras, "Comments on the Feasibility of LES for Wings, and on a Hybrid RANS/LES Approach." Advances in DNS/LES, 1st AFOSR Int. Conf. on DNS/LES, Greyden Press, Columbus, H., Aug. 4-8, 1997.

[12] P.R. Spalart, S. Deck, M. Shur, and K.D. Squires, "A New Version of Detached-Eddy Simulation, Resistant to Ambiguous Grid Densities," *Theoritical and Computational Fluid Dynamics*, vol. 20, pp. 181–195, 2006, doi: 10.1007/s00162-006-0015-0.

[13] F.R. Menter, and M. Kuntz, "Adaptation of Eddy-Viscosity Turbulence Models to Unsteady Separated Flow Behind Vehilces, *The Aerodynamics of Heavy Vehicles: Trucks, Buses and Trains, Edited by McCallen, R. Browand, F. and Ross, J.* ," *Springer, Berlin Heidelberg New York, 2004*, 2-6 Dec. 2002.

[14] Wang, B. Y and Zha, G.-C., "Detached-Eddy Simulation of a Co-Flow Jet Airfoil at High Angle of Attack ," *To appear in AIAA Journal of Aircraft, 2011*, 2011.

[15] Wang, B. Y and Zha, G.-C., "Detached-Eddy Simulation of Transonic Limit Cycle Oscillations Using High Order Schemes," *To appear in Journal of Computer & Fluids*, 2011.

[16] Im, H-S., and Zha, G-C., "Delayed Detached Eddy Simulation of a Stall Flow Over NACA0012 Airfoil Using High Order Schemes." AIAA Paper 2011-1297, 49th AIAA Aerospace Sciences Meeting including the New Horizons Forum and Aerospace Exposition 4 - 7 January 2011, Orlando, Florida, submitted to AIAA Journal, 2011.

[17] B. Wang, Z. Hu, and G. Zha, "A General Sub-Domain Boundary Mapping Procedure For Structured Grid CFD Parallel Computation," *AIAA Journal of Aerospace Computing, Information, and Communication*, vol. 5, pp. 425–447, 2008.

[18] P.R. Spalart, and S.R. Allmaras, "A One-equation Turbulence Model for Aerodynamic Flows." AIAA-92-0439, 1992.

[19] G.C. Zha, Y.Q. Shen, and B.Y. Wang, "An improved low diffusion E-CUSP upwind scheme ," *Journal of Computer and Fluids*, vol. 48, pp. 214–220, 2011, doi:10.1016/j.compfluid.2011.03.012.

[20] G.C. Zha, Y.Q. Shen, and B.Y. Wang, "Calculation of Transonic Flows Using WENO Method with a Low Diffusion E-CUSP Upwind Scheme." AIAA Paper 2008-0745, 46th AIAA Aerospace Sciences Meeting, Reno, NV, Jan. 2008.

[21] P. Roe, "Approximate Riemann Solvers, Parameter Vectors, and Difference Schemes," *Journal of Computational Physics*, vol. 43, pp. 357–372, 1981, doi:10.1016/0021-9991(81)90128-5.

[22] J. Edwards, "A Low-Diffusion Flux-Splitting Scheme for Navier-Stokes Calculations," *Computer & Fluids*, vol. 6, pp. 635–659, 1997, doi:10.1016/S0045-7930(97)00014-5.

[23] B.Y. Wang, and G.C. Zha, "Comparison of a Low Diffusion E-CUSP and the Roe Scheme for RANS Calculation." AIAA Paper 2008-0596, 46th AIAA Aerospace Sciences Meeting and Exhibit, Jan. 7-10, 2008.

[24] Shen, Y.Q., and Zha, G.C., "Improvement of the WENO Scheme Smoothness Estimator," *International Journal for Numerical Methods in Fluids*, vol. 64,, pp. 653–675, 2009, doi:10.1002/fld.2186.

[25] Shen, Y.Q., Zha, G.C., and Wang, B.Y., "Improvement of Stability and Accuracy of Implicit WENO Scheme," *AIAA Journal*, vol. 47, pp. 331–334, 2009, doi:10.2514/1.37697.

[26] Y.Q. Shen, B.Y. Wang, and G.C. Zha, "Implicit WENO Scheme and High Order Viscous Formulas for Compressible Flows ." AIAA Paper 2007-4431, 2007.

[27] A. Jameson, "Time Dependent Calculations Using Multigrid with Applications to Unsteady Flows Past Airfoils and Wings." AIAA Paper 91-1596, 1991.

[28] E.C. Yates Jr., "AGARD standard aeroelastic configurations for dynamic response. Candidate configuration I.-wing 445.6 ." NASA-TM-1000492, 1987.

[29] R.V. Goggett, R.V. Rainey, and H.G. Morgan, "An experimental investigsation of Aerodynamic Effects of Airfoil Thickness on Transonic Flutter Characteristics." NASA TMX-79, 1959.

[30] M.A. Bakhle, T.S.R. Reddy, and T.G. Keith Jr., "Time Domain Flutter Analysis of Cascades Using a Full-Potnetial Solver," *AIAA Journal*, vol. 30, pp. 163–169, 1992, doi: 10.2514/3.10896.

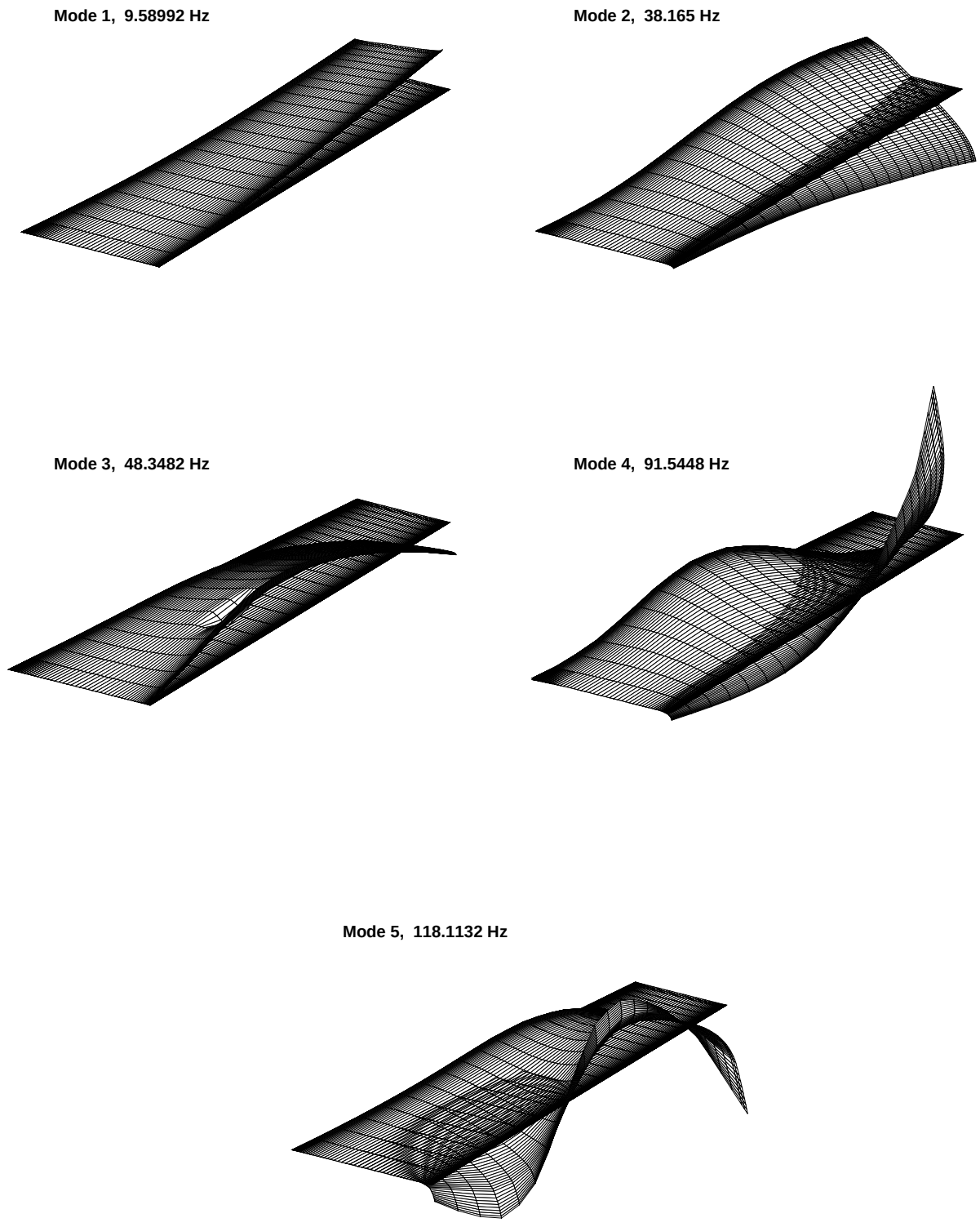

Figure 2: Five modal deflections for AGARD Wing 445.6 Weakend 3[28]; mode 1(top left), mode 2(top right), mode 3(middle left), mode 4(middle right), mode 5(bottom)

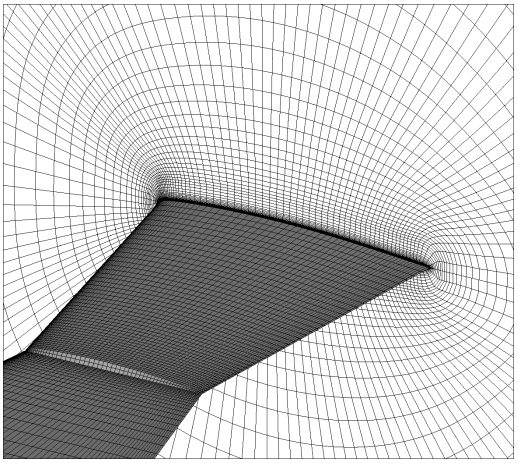

Figure 3: Computational mesh of 137×91×70 for AGARD Wing 445.6 Weakend 3

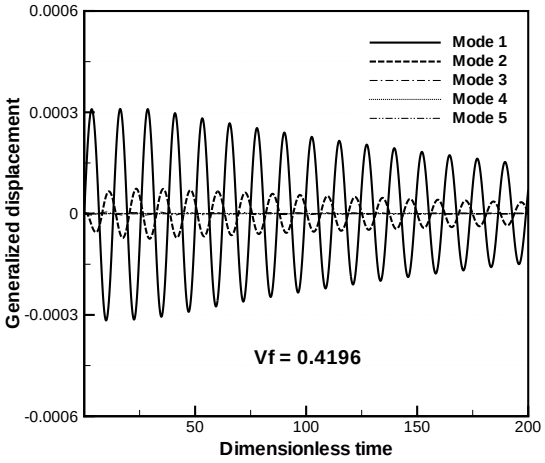

Figure 5: Damped response of the AGARD Wing flutter; $M = 0.678$, $V_f = 0.4196$

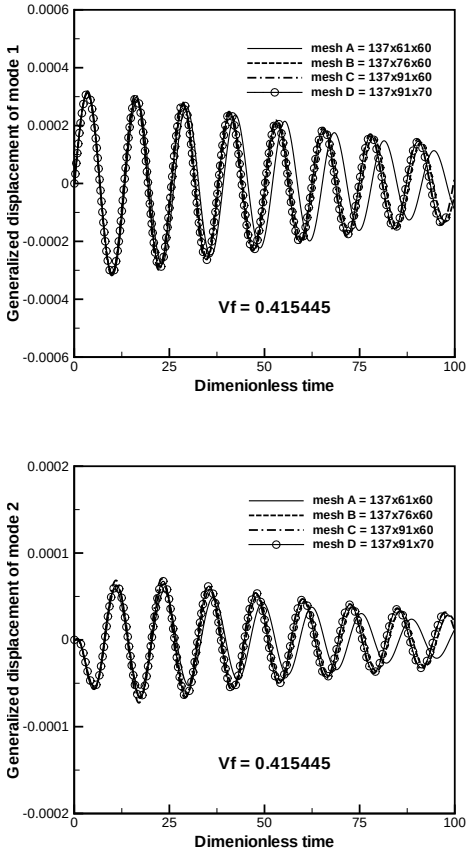

Figure 4: Mesh convergence test for the AGARD Wing flutter; $M = 0.678$, $V_f = 0.415445$

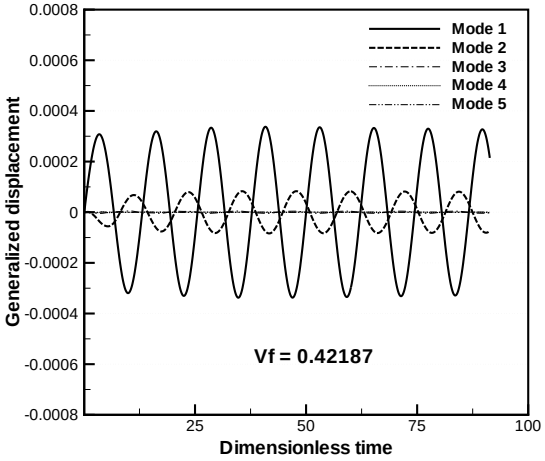

Figure 6: Neutral response of the AGARD Wing flutter; $M = 0.678$, $V_f = 0.42187$

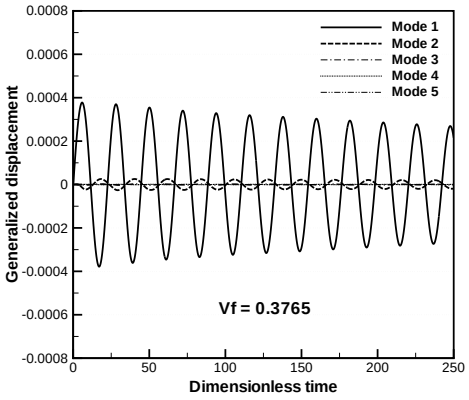

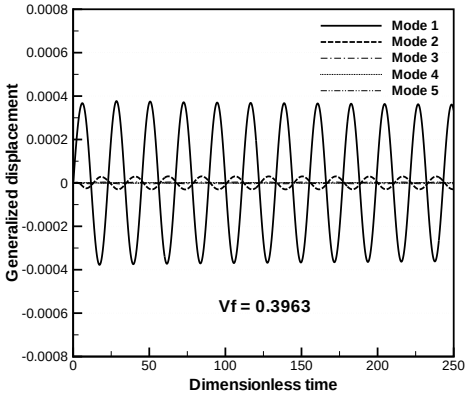

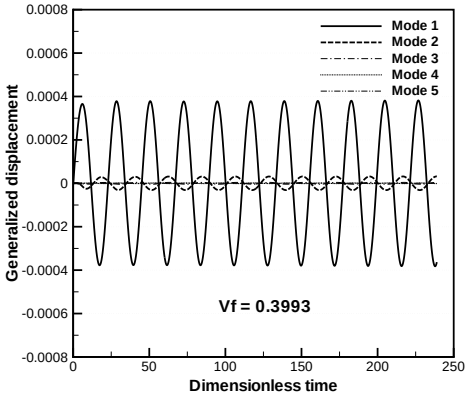

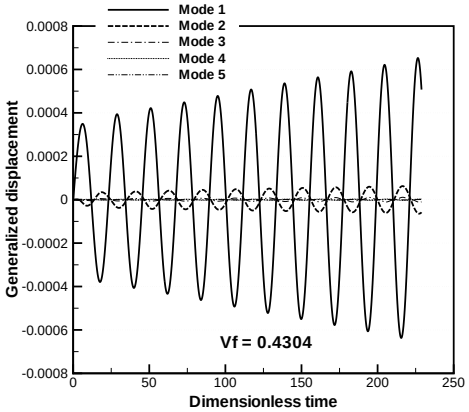

Figure 7: Modal displacements of the AGARD Wing flutter for $M = 1.141$

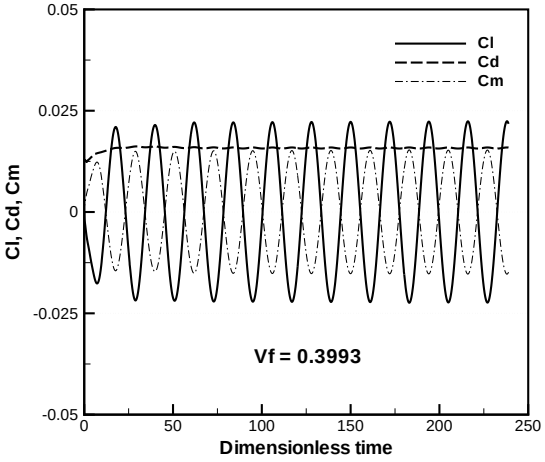

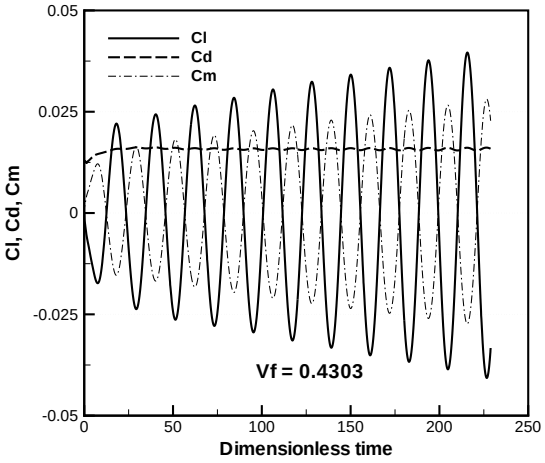

Figure 8: Predicted lift(C_l),drag(C_d), and momentum coefficients(C_m) of the AGARD Wing at the supersonic flutter boundary; $V_f = 0.3993$(top), $V_f = 0.4304$(bottom)

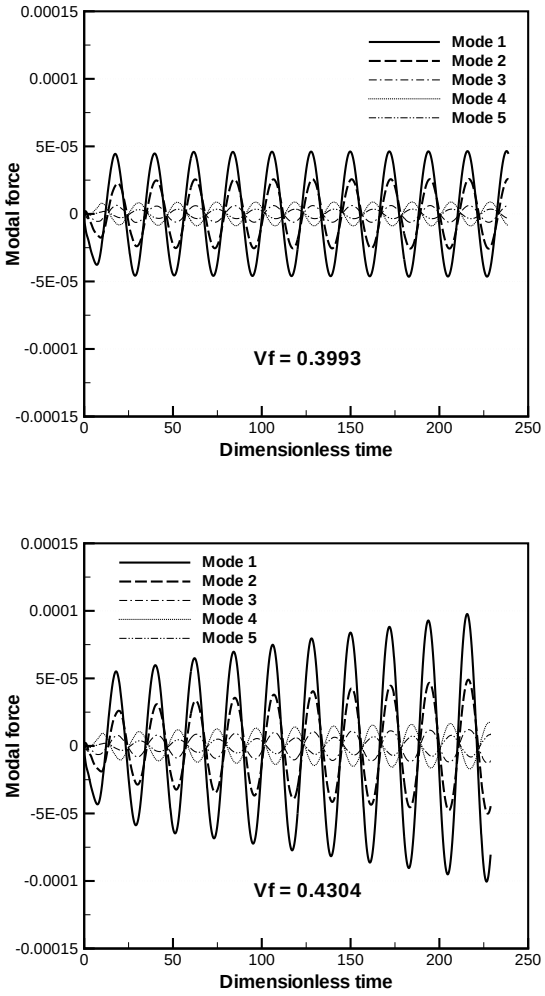

Figure 9: Predicted modal force $(\frac{\tilde{\phi}_j^{*T}}{m_j^*} \cdot \mathbf{F}^* \cdot {V_f}^2 \cdot \frac{b_s^2 L}{V} \cdot \bar{m})$ of the AGARD Wing at the supersonic flutter boundary; $V_f = 0.3993$(top), $V_f = 0.4304$(bottom)

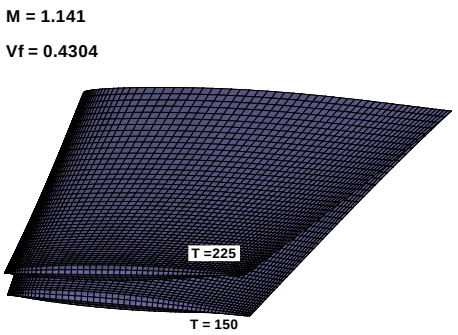

Figure 10: Wing fluttering from the fully coupled FSI simulation for $M = 1.141$ and $V_f = 0.4304$

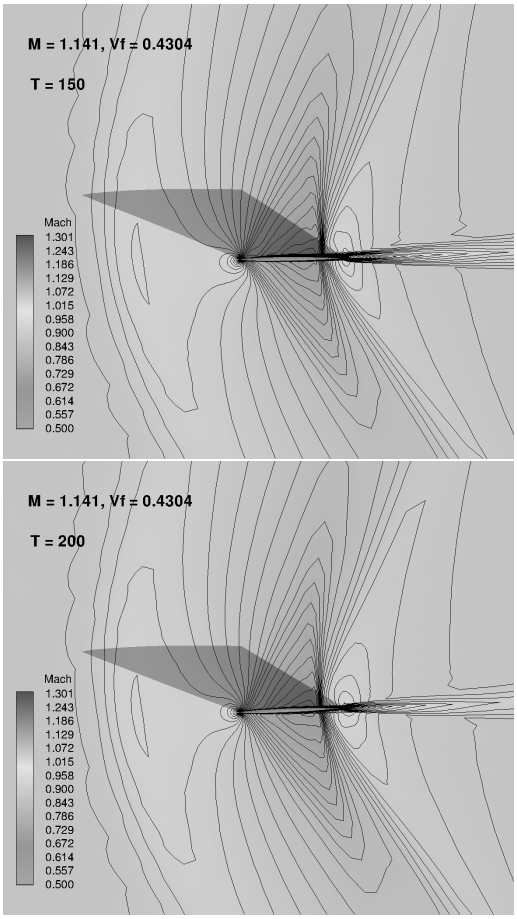

Figure 11: Instantaneous Mach number at tip section for $M = 1.141$ and $V_f = 0.4304$; T=150(top), T=200(bottom)

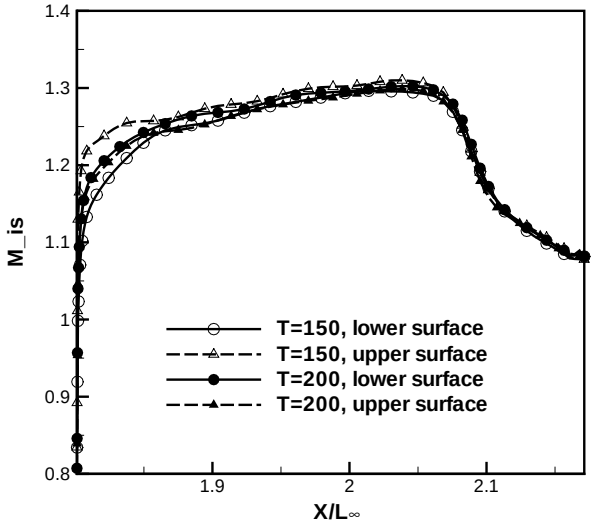

Figure 12: Variation of surface isentropic Mach number at tip section during the supersonic flutter for $M = 1.141$ and $V_f = 0.4304$

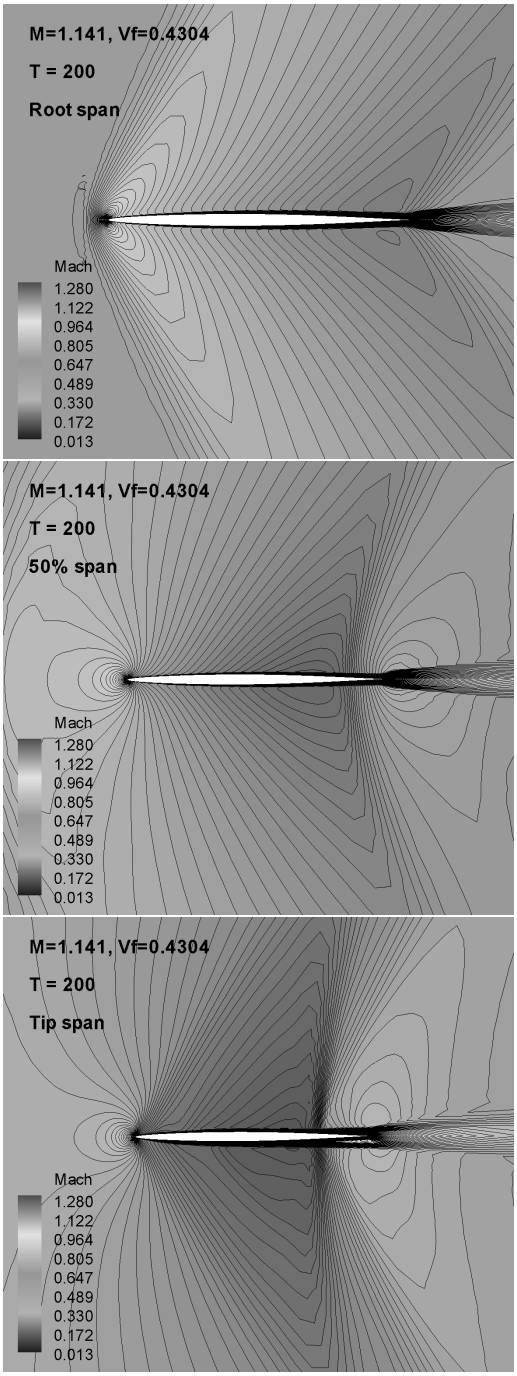

Figure 13: Instantaneous Mach number at T=200 for $M = 1.141$ and $V_f = 0.4304$; root span(top), 50% span(middle), tip span(bottom)

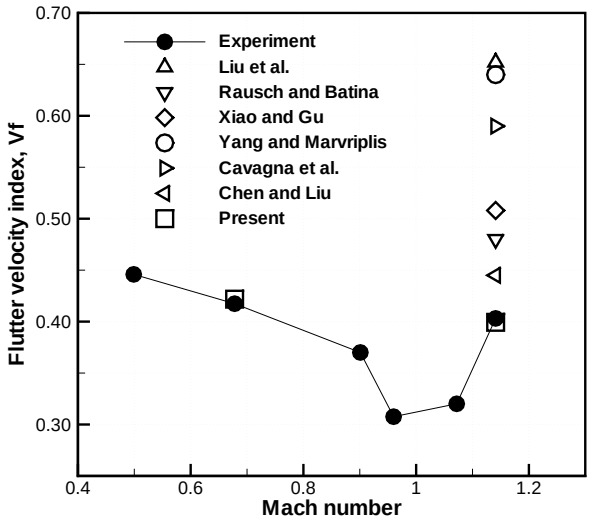

Figure 14: Flutter velocity index of AGARD Wing 445.6 Weakend 3